Journal of Physical Science Vol. 36(2), 99-111, 2025



# The Incorporation of Zn Metal into SnS and Its Impact on Photocatalytic Performance

Aya Ahmed, Essam Ahmed Abdel-whab, Farid M. Abdel-Rahim, Abdelaziz M. Aboraia\*

Physics Department, Faculty of Science, Al-Azhar University, Assiut Branch, 71524, Egypt

\*Corresponding author: a.m.aboraia@gmail.com

Published online: 29 August 2025

**To cite this article:** Ahmed, A. et al. (2025). The incorporation of Zn metal into SnS and Its Impact on Photocatalytic Performance. *J. Phys. Sci.*, 36(2), 99–111. https://doi.org/10.21315/jps2025.36.2.6

To link this article: https://doi.org/10.21315/jps2025.36.2.6

**ABSTRACT:** Investigation of the addition of zinc atoms into tin sulfide crystals to boost their performance for environmental use as a photocatalyst. We examine the development methods, physical characteristics and light absorption capabilities of tin sulfide (SnS) materials with zinc additives. A high-temperature solid-state approach allowed researchers to introduce different amounts of Zn into the SnS crystal structure, followed by X-ray diffraction (XRD), scanning electron microscope (SEM) and energy dispersive X-ray analysis (EDX), as well as UV-visible spectroscopy characterisation. The band gap widening effect from Zn doping SnS enables better light absorption across the visible spectrum since the energy gap decreases from 1.043 eV to 1.039 eV. The photocatalytic degradation tests of methylene blue (MB) as a pollutant model demonstrated that Zn-doped SnS outperforms pure SnS as a photocatalyst. The Zn-doped SnS enhanced the photocatalytic performance from 88% to 92% in 120 minutes due to superior charge carrier dissociation and inhibited electron-hole recombination. This work demonstrates Zn-doped SnS potential as an effective photomaterial for wastewater management and environmental cleanup systems through its cost-efficient design.

**Keywords:** Zn-doped SnS, Nanoparticles, Photocatalysis, Visible light, Degradation, Methylene blue

## 1. INTRODUCTION

Photocatalysis proved to be a very promising technology for solving many environmental and energy issues, such as water treatment and air treatment, and producing renewable energy. 1-3 One of them is the search for efficient photocatalysts that would help to transmute the sun's rays into chemical reactions. Among all the photocatalytic materials, tin (II) sulphide (SnS) nanoparticles have drawn much attention in recent years for their non-toxicity, abundance in the earth and appropriate band gap energy for visible light absorption. 4,5 The semiconductor material SnS shows unique properties making it a suitable candidate for applications in photocatalysis

and photovoltaics and optoelectronics. SnS has a direct band gap of around 1.3 eV to 1.5 eV, which is ideal for absorbing visible light, making it a strong candidate for solar-driven photocatalysis and indirect band gap ranged from 1.0eV to 1.1 eV.<sup>6,7</sup>

However, the use of SnS in photocatalysis in real-life scenarios is faced with some challenges, which are a low absorption coefficient, very short lifetimes of photogenerated charges, and a low surface area that accommodates the catalytic reaction. <sup>8,9</sup> To overcome these limitations, doping of SnS with various metal ions has been tried as an effective method. <sup>10–12</sup> Doping is a process in which a foreign atom is introduced into the crystal lattice of the host material, which brings changes to the electrical, mechanical and optical characteristics of the material. <sup>13,14</sup> Among all dopants, zinc (Zn) is one of the best-studied dopants used to improve the photocatalytic activity of semiconductors. <sup>15–17</sup> Zn is known to alter the electronic structure favourably and enhance the carrier dynamics in the host materials, making Zn a candidate for doping SnS nanoparticles. <sup>18</sup> However, several compositions based on sulphur, like Ag-Ag<sub>2</sub>S-CdS nanowires, noted that the degradation efficiency increased from 12.5% to 57.0% in the neutral, 40.6% to 80.1% in the alkaline and 91.9% to 97.9% in the acid environment under the influence of sunlight. <sup>19,20</sup>

The main research question of this study is whether Zn doping has a positive impact on the photocatalytic activity of SnS nanoparticles through the modification of light absorption capacity, a decrease in the rate of recombination of photo-generated electron and hole charges and provision of additional active sites for the photocatalytic processes. The present study aims to prepare the Zn-doped SnS nanoparticles by melt quenching, analyse the structure and optical properties of the synthesised nanoparticles and, also monitor the photocatalytic activity of the synthesised nanoparticles under visible light illumination. By achieving these outcomes, this research aims to contribute to the development of efficient and sustainable photocatalytic materials for environmental and energy applications. The findings of this study could pave the way for further exploration of doped SnS nanoparticles and their potential applications in photocatalysis and beyond.

## 2. EXPERIMENTAL

## 2.1 Synthesis of Zn-Doped SnS

Highly pure powders of Sn (99.99%), sulphur (S) (99.99%) and Zn (99.99%) were combined in a stoichiometric ratio ( $Sn_{60}S_{40} = 0.6$  gm Sn + 0.4 gm S,  $Sn_{48}Zn_{12}S_{40} = 0.48$  gm Sn + 0.12 gm Zn + 0.40 gm S;  $Sn_{44}Zn_{18}S_{40} = 0.44$  gm Sn + 0.18 gm Zn + 0.40 gm S) and placed inside an ampoule. The ampoule was then evacuated to a pressure of  $10^{-5}$  Torr and sealed. To ensure a uniform mixture along the length of

the ampoule, it was vigorously shaken. The sealed ampoule was placed in a horizontal furnace, where the temperature was gradually increased to 1,000°C at a rate of 20°C per h. It was maintained at this temperature for 24 h to allow proper reaction and homogenisation. Afterwards, the ampoule was slowly cooled to room temperature, yielding a free-flowing, shiny and homogeneous polycrystalline powder.<sup>21,22</sup>

## 2.2 Characterisation Techniques

X-ray diffraction (XRD) patterns of SnS were recorded by LANScientific X-ray diffractometer-FINE (LANScientific Co. Ltd., China) using CuK $\alpha$  ( $\lambda$  = 0·154056 nm) radiation with 20 in the range 10°–80°. The lateral morphology of active materials was studied utilising SEM (JSM 5400 LV, Switzerland). The optical absorption and energy gap were performed in the wavelength range of 200 nm to 1,000 nm using a Jasco V670 ultraviolet-visible (UV-Vis) spectrophotometer (Jasco Company, Italy) at room temperature.

#### 2.3 Photodegredation

The efficiency of using sunlight by the specimens was determined by the reduction in the concentration of methylene blue (MB) in water under artificial sunlight. A 40 mL MB solution of 5 mgL<sup>-1</sup> concentration was prepared in a photochemical reactor and then 30 mg of photocatalyst was added to start degradation. The solution was then allowed to stir under dark conditions for 60 min to enhance the adsorption-desorption balance. The photocatalytic performance of the samples was examined under natural sunlight, which was mimicked by a 500 W Xe lamp placed 15 cm above the solution. At each irradiation time, 2 mL aliquots were taken and subjected to centrifugation and then the absorbance of the MB was determined at its retrieval maximum wavelength of 664 nm. For additional confirmation of the improved activity of the synthesised catalyst with respect to pure SnS under visible light irradiation, the experiment was performed using visible light only, filtered at 420 nm. The MB removal efficiency was established with the percentage removal formula expressed in Equation 1 to show the level of degradation.<sup>23</sup>

$$R\% = \left(\frac{C_0 - C_t}{C_0}\right) \times 100\tag{1}$$

#### 3. RESULT AND DISCUSSION

Figure 1 shows the XRD pattern of pure SnS nanoparticles typically shows characteristic peaks corresponding to orthorhombic SnS. Key diffraction peaks are observed at specific 20 values, such as 110, 101, 111, 211, 131, corresponding to

 $2\theta = 31.5^{\circ}$ ,  $32^{\circ}$ ,  $38.7^{\circ}$ ,  $50.3^{\circ}$  and  $52.5^{\circ}$ , respectively.<sup>24</sup> These peaks match well with the standard International Center for Diffraction Data (ICCD) card for orthorhombic SnS (ICCD pattern no. 00-039-0354), confirming the phase purity and crystallinity of the synthesised SnS nanoparticles.<sup>25,26</sup> Upon doping SnS with Zn, several changes in the XRD patterns are typically observed, for instance, peak shifts, since the diffraction peaks of Zn-doped SnS nanoparticles may exhibit slight shifts compared to pure SnS. These shifts are due to the incorporation of Zn<sup>2+</sup> ions into the SnS lattice. Zn<sup>2+</sup> has a smaller ionic radius (0.74 Å) compared to Sn<sup>2+</sup> (0.93 Å), which can cause lattice contraction and result in peak shifts to higher  $2\theta$  values.

The XRD peak intensities reduced while the full width at half maximum value changed from narrow to broad as the Zn concentration increased. A decrease in crystallite size happens because Zn<sup>2+</sup> ions replace Sn<sup>4+</sup> ions within the SnS crystal structure. The accumulation of Zn ions partially at grain boundaries disrupts crystal growth, which potentiates peak broadening and the reduction of peak intensity, as shown in Table 1. The absence of new peaks indicates that Zn is well-dispersed within the SnS structure without forming significant amounts of secondary phases.

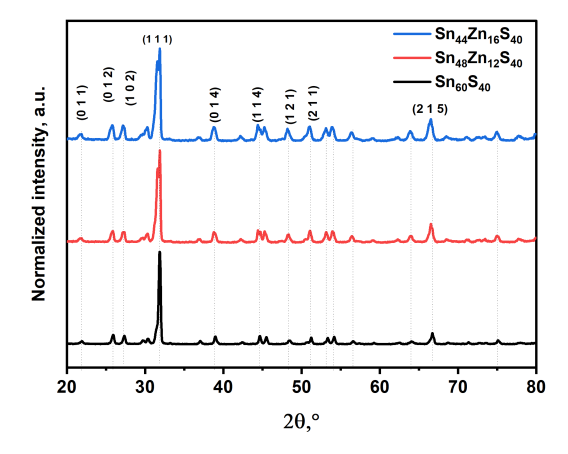


**Figure 1:** XRD patterns of  $Sn_{60}S_{40}$ ,  $Sn_{48}Zn_{12}S_{40}$  and  $Sn_{44}Zn_{18}S_{40}$ .

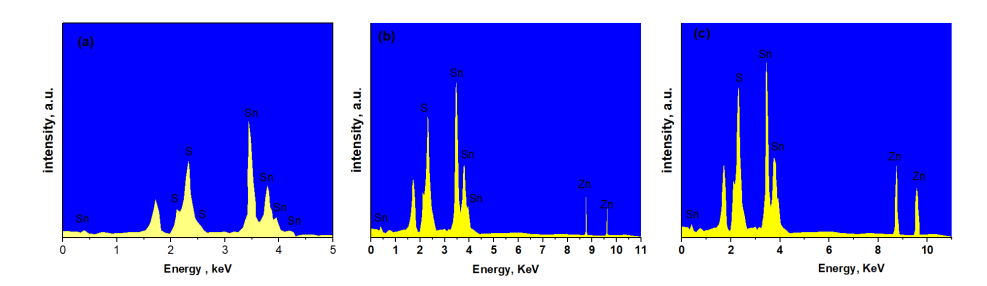


Figure 2 : EDAX pattern of (a)  $Sn_{60}S_{40}$ , (b)  $Sn_{48}Zn_{12}S_{40}$  and (c)  $Sn_{44}Zn_{16}S_{40}$ .

Table 1: Crystalline size, strain, and dislocation density of SnS doped Zn

Samples	Size (nm)	Strain	Dislocation density (nm <sup>-2</sup> )
$Sn_{60}S_{40}$	86	34	$1.33 \times 10-4$
$Sn_{48}Zn_{12}S_{40}$	74	47	$1.82 \times 10-4$
$Sn_{44}Zn_{16}S_{40}$	72	48	$1.87 \times 10-4$

The crystalline size of Zn-doped SnS nanoparticles can be estimated using the Williamson and Hall equation: <sup>27–29</sup>

$$\beta \cos \theta = \frac{k\lambda}{D} + 4\varepsilon \sin \theta \tag{2}$$

where D is the crystalline size, is the microstrain, k is the shape factor (typically 0.9),  $\lambda$  is the wavelength of the X-ray source (Cu K $\alpha$ , 0.15406 nm), is the full width at half maximum (FWHM) of the diffraction peak and 20 is the Bragg angle. An increase in Zn substitution amounts corresponds to increase strain ( $\epsilon$ ) and dislocation density ( $\delta$ ) levels within synthesised SnS nanoparticles, thereby indicating changes in crystal symmetry as shown in Table 1.

Table 2 presents the EDAX spectrum of the SnS compound, which confirms the presence of Sn, Zn and S. The quantitative analysis reveals that the compound consists of 40% S and 59% Sn, resulting in a stoichiometric ratio of Sn/S at 99. Additionally, the Table 2 demonstrates that Zn is incorporated into Sn at ratios of 12 and 16, as shown in Figure 2. The surface morphology of the synthesised material was analysed using SEM studies. As Figure 3 shows the SEM micrographs of Zn-doped SnS. Due to SnS's regular behaviour, the pristine sample shows erratic nanoparticle distribution with noticeable agglomeration while keeping typical SnS aggregation patterns. The production of voids and pores in the undoped sample can be attributed to rapid gas discharge during the combustion synthesis reaction. An increase in Zn doping causes the porosity to decrease and the void density to decrease because Zn doping suppresses gas evolution while stabilising microstructures during formation.<sup>30,31</sup>

Samples	Atomic weight (%)				
	Sn	Zn	S		
Sn <sub>60</sub> S <sub>40</sub>	59	0	40		
$Sn_{48}Zn_{12}S_{40}$	49	10	41		
$Sn_{44}Zn_{16}S_{40}$	43	19	38		

Table 2: EDAX analysis of SnS doped Zn.

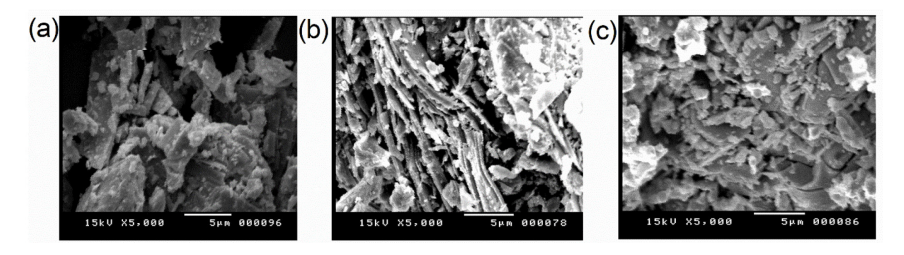


Figure 3: Photo SEM of (a)  $Sn_{60}S_{40}$ , (b)  $Sn_{48}Zn_{12}S_{40}$  and (c)  $Sn_{44}Zn_{16}S_{40}$ .

## 3.1 Optical and Electronic Properties

UV-Vis spectroscopy is a valuable technique for assessing the ability of materials to absorb light. The spectra obtained from the samples in Figure 4(a) demonstrate that all of them exhibit significant absorption of light across a wide range, spanning from the UV region to the near-infrared (NIR) region. From Figure 3(a), absorption edges of pure  $Sn_{60}S_{40}$   $Sn_{48}Zn_{12}S_{40}$  and  $Sn_{44}Zn_{16}S_{40}$  were estimated to be approximately 1,188 nm, 1,192 nm and 1,193 nm, respectively. From Tauc plots, depicted in Figure 4(b), the corresponding band gaps are estimated to be 1.043 eV, 1.04 eV and 1.039 eV, by applying the Tauc equation:<sup>32</sup>

$$\alpha(hv)^n = k (hv - E_{\rho}) \tag{3}$$

where, h and denote the diffuse absorption coefficient, the Planck constant, and the frequency; n can be determined by the indirect gap (= 1/2) or direct gap (= 2) types. The relatively small differences in band gaps indicate that the effectiveness of their photocatalytic performance is primarily influenced by visible light. The value of ban gap decreases when Zn concentration levels increase. The band gap reduction occurs because of Zn doping which creates free radicals and new chemical bonds and introduces localised energy states to the band structure.<sup>33</sup>

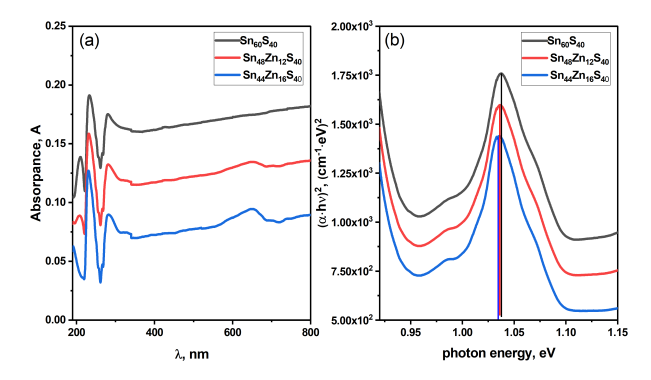
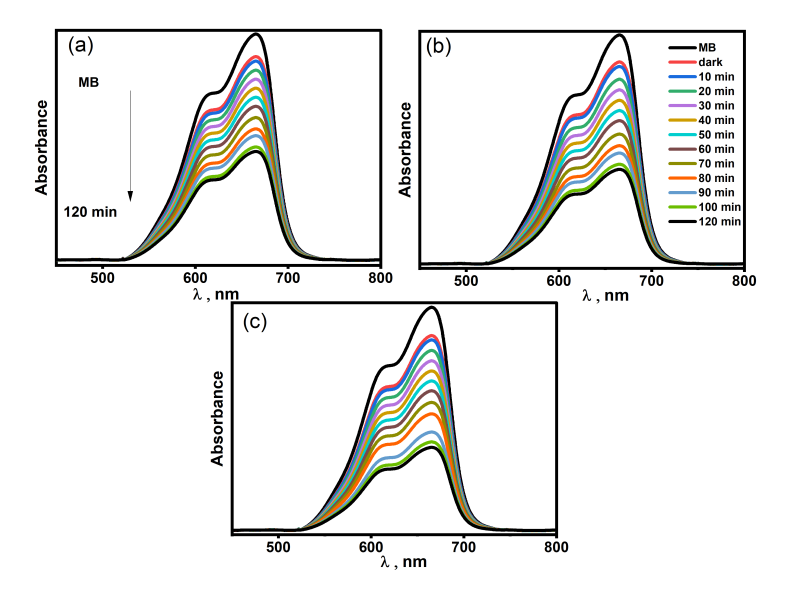


Figure 4: (a) UV-Vis spectrum and (b) energy gap of Sn<sub>60</sub>S<sub>40</sub>, Sn<sub>48</sub>Zn<sub>12</sub>S<sub>40</sub> and Sn<sub>44</sub>Zn<sub>18</sub>S<sub>40</sub>

# 3.2 Photocatalytic Degradation of Organic Dyes

In this study, we explored the photocatalytic degradation of MB dye using pristine SnS and Sn combined with varying amounts of Zn under light exposure. The goal was to evaluate the effectiveness of these materials as photocatalysts, which utilise light to drive chemical reactions, in removing MB dye—a representative of positively charged dyes—from water. The MB dye solution was highly diluted (4% moles per liter) and exhibited maximum light absorption at a wavelength of 664 nm. The experiments were conducted under UV light, and the results, depicted in Figure 5, were monitored over a 120-min irradiation period.



**Figure 5:** Photodegradation of (a)  $Sn_{60}S_{40}$ , (b)  $Sn_{48}Zn_{12}S_{40}$ , and (c)  $Sn_{44}Zn_{18}S_{40}$ .

This may most probably be because of the effects of light and other oxidising agents, which cause the coloured dyes in this experiment to fade. Comparing the efficiency of the tested materials  $Sn_{44}Zn_{16}S_{40}$  was established as the most effective photocatalyst for the degradation of pollutants when exposed to light. A general procedure of photocatalytic degradation of MB dye using SnS and Sn with different concentrations of Zn has been presented as follows: as in the case of MB dye degradation, which is used as an example, the process is most likely to have a specific pattern based on which the rate of degradation depends on the concentration of the remaining dye, as demonstrated in Figure 5. The result of the experiment proves that the dye degradation conforms to a reaction model close to the first-order reaction and is expressed in the equation:  $^{34,35}$ 

$$Ln\left(\frac{C_o}{C_t}\right) = K_1.t \tag{4}$$

 $C_o$  and  $C_t$  stand for starting and remaining concentrations of MB at the particular illumination time before determining  $K_1$ , which represents the first-order rate constant. This conclusion is in agreement with the interaction between  $C_o$  and C with time and the linear trend line of the graph, In  $(C_o/C)$  against time.

When we incorporated different amounts of zinc into SnS, the photocatalytic activity of these SnS NCs increased, and they degraded the dye molecules under visible light. These photocatalysts also revealed excellent degradation efficiency of dyes in the present study, and the 120 min irradiation period confirmed the effectiveness of these systems for the degradation of pollutants.

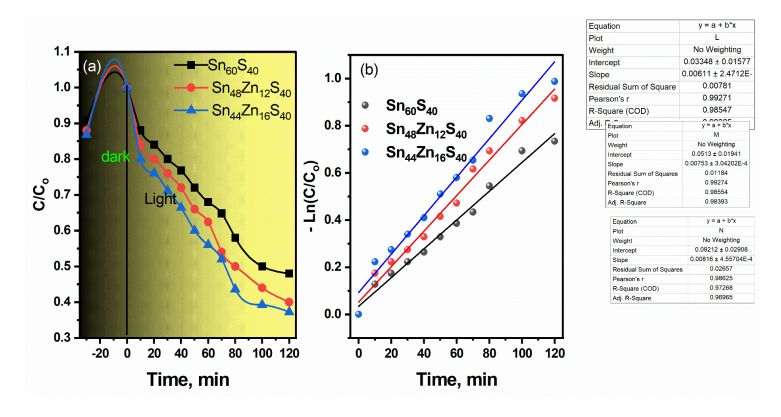


**Figure 6:** (a)  $(C/C_o)$  of  $Sn_{60}S_{40}$ ,  $Sn_{48}Zn_{12}S_{40}$  and  $Sn_{44}Zn_{18}S_{40}$ , and (b) k constant of  $Sn_{60}S_{40}$ ,  $Sn_{48}Zn_{12}S_{40}$  and  $Sn_{44}Zn_{16}S_{40}$ .

The changes in  $C/C_0$  of MB dye concentration are depicted in Figure 6(a), where the gradual discharge of the dye over time under UV light exposure is well shown. The SnS photocatalyst completed the degradation of MB within 120 min, with the attributed contribution from the charge carrier reactive process. Nevertheless, introducing Zn doping improved the photocatalytic activity tremendously, and enhanced the overall dye removal efficiency from 88% to 92% within the same period as indicated in Figure 6(a). Furthermore, the photocatalytic degradation of MB dye in the presence of SnS photocatalyst also obeys pseudo-first-order kinetics as depicted from the plot of  $(-\ln[C/C_0])$  vs t (Figure 6[b]). From the pseudo-first-order kinetic model applied to the degradation of MB by SnS, the pseudo-first-order rate constant was determined to be  $6.11 \times 10^{-3} \, \mathrm{min^{-1}}$ . Nonetheless, Zn-doped SnS have comparable rate constants that amounted to  $7.53 \times 10^{-3} \text{ min}^{-1}$  and  $8.16 \times 10^{-3} \text{ min}^{-1}$  as shown in Figure 6(b). This improved performance is due to the increased charge separation thus leading to the generation of highly active oxidising species such as hydroxyl radical (HO·) and superoxide radical (O<sub>2</sub>• -). These radicals, in fact, reduce the pollutant molecules, thus increasing the photocatalytic trait.

Table 3: The energy gap, k constant and chi-square of  $Sn_{60}S_{40}$ ,  $Sn_{48}Zn_{12}S_{40}$  and  $Sn_{44}Zn_{16}S_{40}$ .

Samples	Energy gap (eV)	K (min <sup>-1</sup> )	R <sup>2</sup>
$Sn_{60}S_{40}$	1.043	0.00611	98.5
$Sn_{48}Zn_{12}S_{40}$	1.040	0.00753	98.3
$Sn_{44}Zn_{16}S_{40}$	1.039	0.00816	98.0

## 3.3 Mechanism of MB Dye Degradation

In the photocatalytic process, when SnS absorbs a photon, an electron is excited from the valence band to the conduction band, creating an electron-hole pair. The electrons in the conduction band of SnS interact with oxygen  $(O_2)$  to generate superoxide radicals  $(O_2^-)$ , while the holes  $(h^+)$  react with hydroxide ions  $(OH^-)$  and water  $(H_2O)$  to form hydroxyl radicals (OH). These highly reactive radicals then interact with ionised dye molecules, breaking them down into less harmful substances such as smaller hydrocarbons, water  $(H_2O)$ , and carbon dioxide  $(CO_2)$ . Additionally, the strong oxidising holes  $(h^+)$  can directly contribute to the breakdown of MB dye molecules. The overall mechanism of MB degradation under visible light irradiation is illustrated in Figure 7.

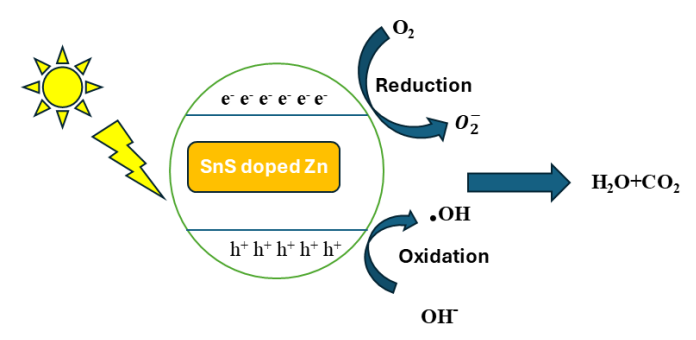


Figure 7: The mechanism of visible light photocatalytic degradation of MB over the SnS.

#### 4. CONCLUSION

Synthesis of Zn-doped SnS nanopowders with different Zn proportions (0 wt.%, 12 wt.% and 16 wt.%) occurred successfully through the melt quenching technique. A detailed examination of Zn doping impact was conducted for structural properties, together with morphological analysis and photocatalytic behaviour assessment. The crystallite dimensions of Zn-doped SnS decreased when Zn doping concentration increased. The photocatalytic performance of pure SnS on MB dye removal significantly increased after Zn doping because it reached 92% removal efficiency during 120 min of photocatalytic reaction time. Pseudo-first-order rate constants for SnS<sub>2</sub> increased from  $6.11 \times 10^{-3}$  min<sup>-1</sup> to higher values of  $7.53 \times 10^{-3}$  min<sup>-1</sup> and  $8.16 \times 10^{-3}$  min<sup>-1</sup> after Zn doping was applied to the material. The identified photocatalytic properties of Zn-doped SnS nanopowders show their high ability to remove organic contaminants by providing potential solutions for magnetic device applications.

#### 5. ACKNOWLEDGEMENTS

Thanks for physics department, faculty of science, Al-Azhar university, Assiut branch and its laboratories.

#### 6. REFERENCES

 Aboraia, A. M. et al. (2023). A heterostructural MoS<sub>2</sub>QDs@UiO-66 nanocomposite for the highly efficient photocatalytic degradation of methylene blue under visible light and simulated sunlight. RSC Adv., 13(49), 34598–34609. https://doi.org/10.1039/ D3RA06299F

- Aboraia, A. M.et al. (2024). Comparison study between as-synthesized ZnO and ZnO derived from ZiF-8 metalorganic framework in removing methylene blue. *Mod. Phys. Lett. B*, 38(24), 2450221. https://doi.org/10.1142/S021798492450221X
- 3. Ahmad, A. L. et al. (2024). Influence of TiO<sub>2</sub> phases and operational parameters on photocatalytic degradation of methyl orange. *J. Phys. Sci.*, 35(2), 65–82. https://doi.org/10.21315/jps2024.35.2.5
- 4. Ahmad, I. et al. (2023). Sn-based materials in photocatalysis: A review. *Adv. Colloid Interface Sci.*, 321, 103032. https://doi.org/10.1016/j.cis.2023.103032
- 5. Arulanantham, A. M. S. et al. (2025). Influence of sulfur concentration on phase formation in SxnSy thin films deposited through nebulizer spray pyrolysis technique. *Appl. Phys. A*, 131(1), 1–14.
- Baby, B. H., & Amrutha, E. G. (2020). The formation of orthorhombic SnS nanorods using CTAB in solvothermal method with its phase stability, optical and electrical properties. *Mater. Res. Bull.*, 128, 110883. https://doi.org/10.1016/j.materresbull.2020.110883
- 7. Bae, S.-R. et al. (2011). Sn-Ge-S composites prepared by melt-quenching method as an anode material for Li-secondary batteries. *Meet. Abstr.* MA2011-02 654.
- 8. Baishya, K. et al. (2018). Graphene-mediated band gap engineering of WO 3 nanoparticle and a relook at Tauc equation for band gap evaluation. *Appl. Phys. A*, 124, 1–6.
- 9. Butova, V. V. et al. (2021). The joint effect of naphthalene-system and defects on dye removal by UiO-66 derivatives. *Microporous Mesoporous Mater.* 325, 111314. https://doi.org/10.1016/j.micromeso.2021.111314
- 10. Etefagh, R., Shahtahmasebi, N., & Karimipour, M. et al. (2013). Effect of Zn doping on optical properties and photoconductivity of SnS<sub>2</sub> nanocrystalline thin films. *Bull. Mater. Sci.*, 36(3), 411–416.
- 11. Gahramanli, L. R. et al. (2024). Ag–Ag2<sub>s</sub>–CdS nanostructures: Formation, physical characteristics and role in methylene blue removal. *J. Mater. Sci.: Mater. Electron.* 35(27), 1799. https://doi.org/10.1007/s10854-024-13539-8
- 12. Gahramanli, L. R. et al. (2024). Enhanced adsorption and degradation kinetics of methylene blue by Ag–Ag<sub>2</sub>S–CdS hybrid nanowires. *Opt. Mater.* 154, 115760. https://doi.org/10.1016/j.optmat.2024.115760
- 13. Guo, X. et al. (2023). Review on the advancement of  $SnS_2$  in photocatalysis. *J. Mater. Chem. A.*, 11(14), 7331–7343. https://doi.org/10.1039/D2TA09741A
- 14. He, K. et al. (2018). Method for determining crystal grain size by X-ray diffraction. *Cryst. Res. Technol.*, 53(2), 1700157. https://doi.org/10.1002/crat.201700157
- 15. Henry, J. et al. (2015). Structural and optical properties of SnS nanoparticles and electron-beam-evaporated SnS thin films. *J. Exp. Nanosci.*, 10(2), 78–85. https://doi.org/10.1080/17458080.2013.788226
- 16. Humayun, M. et al. (2022). Recent progress in the synthesis and applications of composite photocatalysts: A critical review. *Small Methods*, 6(2), 2101395. https://doi.org/10.1002/smtd.202101395
- 17. Jasni, N. et al. (2023). Photodegradation of oxytetracycline using fluorescent light driven ZnO quantum dots synthesised via microwave method. *J. Phys. Sci.*, 34(1), 27–41. https://doi.org/10.21315/jps2023.34.1.3

- 18. Khorsand Zak, A. et al. (2011). X-ray analysis of ZnO nanoparticles by Williamson–Hall and size–strain plot methods. *Solid State Sci.*, 13(1), 251–256. https://doi.org/10.1016/j.solidstatesciences.2010.11.024
- 19. Koteeswara Reddy, N. et al. (2015). Review on tin (II) sulfide (SnS) material: Synthesis, properties, and applications. *Crit. Rev. Solid State Mater. Sci.*, 40(6), 359–398. https://doi.org/10.1080/10408436.2015.1053601
- 20. Lather, R., & Jeevanandam, P. (2022). Synthesis of Zn<sup>2+</sup> doped SnS<sub>2</sub> nanoparticles using a novel thermal decomposition approach and their application as adsorbent. *J. Alloys Compd.*, 891, 161989. https://doi.org/10.1016/j.jallcom.2021.161989
- 21. Lei, W. et al. (2022). Zn-doped SnS with sulfur vacancies for enhanced photocatalytic hydrogen evolution from water. *New J. Chem.*, 46(37), 17791–17800. https://doi.org/10.1039/D2NJ03520K
- 22. Li, T. et al. (2024). Flake-like SnS anchored on the carbon layer for supercapacitor electrode with photo-responsive capacitance enhancement. *J. Alloys Compd.*, 976, 173377. https://doi.org/10.1016/j.jallcom.2023.173377
- 23. Liu, Y. et al. (2021). Cu doped SnS<sub>2</sub> nanostructure induced sulfur vacancy towards boosted photocatalytic hydrogen evolution. *Chem. Eng. J.*, 407, 127180. https://doi.org/10.1016/j.cej.2020.127180
- 24. Luo, J. et al. (2022). Phase-controlled synthesis of SnS<sub>2</sub> and SnS flakes and photodetection properties. *J. Phys.: Condens. Matter*, 34(28), 285701. https://doi.org/10.1088/1361-648X/ac6926
- 25. Muniz, F. T. L. et al. (2016). The Scherrer equation and the dynamical theory of X-ray diffraction. *Acta Crystallogr. A: Found. Adv.*, 72(3), 385–390. https://doi.org/10.1107/S205327331600365X
- 26. Muradov, M. et al. (2023). Influence of gamma radiation on structure, morphology, and optical properties of GO and GO/PVA nanocomposite. *Radiat. Phys. Chem.*, 208, 110926. https://doi.org/10.1016/j.radphyschem.2023.110926
- 27. Norton, K. J. et al. (2021). A review of the synthesis, properties, and applications of bulk and two-dimensional tin (II) sulfide (SnS). *Appl. Sci.*, 11(5), 2062. https://doi.org/10.3390/app11052062
- 28. Park, S. et al. (2017). Enhancement of visible-light-driven photocatalytic reduction of aqueous Cr (VI) with flower-like In3\*-doped SnS<sub>2</sub>. *J. Ind. Eng. Chem.*, 45, 206–214. https://doi.org/10.1016/j.jiec.2016.09.024
- 29. Qin, Y. et al. (2020). First-principles calculations combined with experiments to study the gas-sensing performance of Zn-substituted SnS. *Phys. Chem. Chem. Phys.*, 22(31), 17513–17522. https://doi.org/10.1039/D0CP01521K
- 30. Reddy, N. K. et al. (2012). In situ structural studies on orthorhombic SnS micro-crystals. *Eur. Phys. J. Appl. Phys.*, 60(1), 10102. https://doi.org/10.1051/epjap/2012120259
- Sayed, M. M. et al. (2024). The enhanced photocatalytic performance of CPAA doping with different concentrations of Titanium oxide nanocomposite against MB dyes under simulated sunlight irradiations. *Sci. Rep.*, 14(1), 12768. https://doi.org/10.1038/ s41598-024-61983-7

- 32. Son, S.-I. et al. (2020). Effect of working pressure on the properties of RF sputtered SnS thin films and photovoltaic performance of SnS-based solar cells. *J. Alloys Compd.*, 831, 154626. https://doi.org/10.1016/j.jallcom.2020.154626
- 33. Sun, L., et al. (2016). Theoretical perspective on the electronic, magnetic and optical properties of Zn-doped monolayer SnS<sub>2</sub>. *Appl. Surf. Sci.*, 389, 484–490. https://doi.org/10.1016/j.apsusc.2016.07.150
- 34. Zhang, F. et al. (2022). Efficient photocatalytic reduction of aqueous Cr (VI) by Zr<sup>4+</sup> doped and polyaniline coupled SnS<sub>2</sub> nanoflakes. *Sep. Purif. Technol.* 283, 120161. https://doi.org/10.1016/j.seppur.2021.120161
- 35. Zhou, B. et al. (2017). Thermoelectric properties of SnS with Na-doping. *ACS Appl. Mater. Interfaces*, 9(39), 34033–34041. https://doi.org/10.1021/acsami.7b08770